Available online at www.sciencedirect.com
ScienceDirect
Procedia Engineering 102 (2015) 123 – 132
Procedia Engineering
www.elsevier.com/locate/procedia

The 7th World Congress on Particle Technology (WCPT7)

Quadrant and conditional analyses of non-spherical particle segregation in a turbulent channel flow

Derrick O. Njobuenwu*, Michael Fairweather

Institute of Particle Science and Engineering, School of Process, Environmental and Materials Engineering, University of Leeds, Leeds LS2 9JT, UK

Abstract

Turbulent flows transporting particles of different sizes and shapes can be found in many natural and industrial systems. In understanding such flows, it is important to identify the mechanisms responsible for the dispersion, segregation and deposition on solid surfaces of particles with different shapes, and of specific interest here how such particles interact with near-wall coherent turbulent structures (outward motion, ejection, inward motion and sweep). Results from large eddy simulation coupled with Lagrangian particle tracking are used together with conditional statistics (probability density function and scatter plots) in quadrants to study the distribution of fluid, particle and slip velocity fluctuations. The results, though challenging to analyse, give insight into the values of the quadrants and how these distributions reveal the mechanisms responsible for particle segregation in the near-wall region.

Selection and peer-review under responsibility of Chinese Society of Particuology, Institute of Process Engineering, Chinese Academy of Sciences (CAS)

Keywords: Large eddy simulation; turbulence; non-spherical particles; particle segregation; sweep-ejection event

1. Introduction

Understanding and characterising the mechanisms that control the dispersion and segregation of inertial non-spherical particles in a turbulent boundary layer has important implications for many natural and industrial systems, such as solid deposition in marine flows and the deposition of corrosion product in the form of CRUD (corrosion

---

* Corresponding author. Tel.: +44-113-343-2351; fax: 44-113-343-2384.
E-mail address: d.o.njobuenwu@leeds.ac.uk

Selection and peer-review under responsibility of Chinese Society of Particuology, Institute of Process Engineering, Chinese Academy of Sciences (CAS)
doi:10.1016/j.proeng.2015.01.113

residual unidentified deposit) on the outside of the fuel pins in nuclear reactors. Turbulent particle transfer mechanisms in proximity to a solid wall are characterised by complex interactions between turbulence structures and the dispersed phase. Coherent structures (outward motion, ejection, inward motion and sweep) bring particles towards and away from the wall and favour particle segregation in the viscous region, giving rise to non-uniform particle distribution profiles, which peak close to the wall [1]. When particles segregate in specific flow regions, the effect of the dispersed phase on turbulence is no longer negligible since the local particle volume fraction changes. This leads to pockets of high concentrations of particles where the one-way coupling assumption between the particles and the fluid is no longer valid.

This study relies on a precise understanding of the dynamics of particles in a turbulent flow field obtained using large eddy simulation. The translational dynamics of particles is well described by the convection of the particles' centroid in the flow domain. For non-spherical particles, the orientational dynamics must also be considered in order to capture the complete motion of the particles [2]. Jeffery [3] derived an approximate equation of motion for the orientational dynamics of non-spherical particles in the absence of inertia. Jeffery's solution predicts that elongated axisymmetric particles mostly align with the flow direction, but periodically rapidly turn through two-right angles. With much past (e.g. [4-6]), present (e.g. [7-9]) and future research based on Jeffery's equations, it is necessary to study how accounting for particle orientation alters the interaction with turbulent coherent structures and particle segregation in the near-wall region. Fluid, particle and slip velocities are the dynamic parameters used in this work to demonstrate that particle-turbulence interaction is a function of particle shape, inertia and location along the wall-normal axis of a turbulent channel flow. Slip velocity is defined here as the difference in velocity between the fluid and a particle. Statistical analyses of slip velocity have previously appeared in the literature, but only for spherical [10] and prolate [7] particles. The instantaneous and statistical values of the slip velocity fluctuations, together with those of the fluid and the particle, are used herein to characterise particles trapped in ejection-sweep events and particles segregated in near-wall fluid streaks.

2. Mathematical models

2.1. Large eddy simulation

The conservation equations for mass and momentum are decomposed into resolved (large-scale) and unresolved (sub-grid scale) fields using a top-hat filter as this fits naturally into the finite-volume formulation used for solution. The filtered forms of these equations for the resolved scales are given by:

$$\frac{\partial \bar{u}_j}{\partial x_j} = 0, \tag{1}$$

$$\frac{\partial \bar{u}_i}{\partial t} + \bar{u}_j \frac{\partial \bar{u}_i}{\partial x_j} = -\frac{1}{\rho}\frac{\partial \bar{p}}{\partial x_i} - \frac{\partial}{\partial x_j}\left(\bar{\sigma}_{ij} + \tau_{ij}\right), \tag{2}$$

where $\bar{\sigma}_{ij} = -2\nu\bar{s}_{ij}$ and $\tau_{ij} = \overline{u_i u_j} - \bar{u}_i\bar{u}_j$ represent the kinematic viscous stress and the sub-grid scale (SGS) stress tensors, respectively. The unknown SGS stress term required to close these equations was modelled using a dynamic approach [11] which represents the SGS stress as the product of a SGS viscosity and the resolved part of the strain tensor, and is based on the possibility of allowing different values of the Smagorinsky constant at different filter levels. Test filtering was performed in all space directions, with no averaging of the computed model parameter field.

The computations were carried out with the BOFFIN large eddy simulation (LES) code [9, 12]. The code implements an implicit finite-volume incompressible flow solver using Cartesian co-ordinates and a co-located variable storage arrangement. Time advancement is performed using an implicit Gear method for all transport terms with variable time step, and the overall procedure is second-order accurate in space and time. For the convection terms an energy conserving discretization scheme is used and matrix pre-conditioned conjugate gradient methods are employed to solve the equations for pressure and velocity.

2.2. Kinematics and dynamics of a non-spherical particle

The dynamics of an anisotropic particle at time $t + \Delta t$ is fully determined by four non-scalar quantities: the position of its centre of mass, its orientation, and its translational and rotational velocities. Each of these physical quantities changes as a function of time and can be easily represented as a three-component vector, together with orientation, giving a total of thirteen variables.

There are two frames of reference: the inertial (or Eulerian) coordinate system, $\mathbf{x}' = [x', y', z']$, which is a fixed frame of reference, and the particle coordinate system, $\mathbf{x}' = [x', y', z']$, which is a frame of reference with its origin at the particle centre of mass and its axis being the principal axis. The transformation between the inertial frame and the particle frame is expressed as $\mathbf{x}' = \mathbf{A} \cdot \mathbf{x}$ [13]. The transformation matrix $\mathbf{A} = [a_{ij}]$ can be expressed in terms of either Euler angles (ϕ, θ, ψ) or quaternions $\mathbf{q} = (q_1, q_2, q_3, q_0)$ [13]. The Euler angles represent the direction cosines of the particle axes in the inertial frame, as shown in Figure 1. The orientational matrix $\mathbf{A}$ in terms of the quaternion $\mathbf{q}$, subject to the constraint that the sum of the individual components is unity, is given by:

$$\mathbf{A} = \begin{bmatrix} 1 - 2(q_2^2 + q_3^2) & 2(q_1 q_2 + q_3 q_0) & 2(q_1 q_3 - q_2 q_0) \\ 2(q_2 q_1 - q_3 q_0) & 1 - 2(q_3^2 + q_1^2) & 2(q_2 q_3 + q_1 q_0) \\ 2(q_3 q_1 + q_2 q_0) & 2(q_3 q_2 - q_1 q_0) & 1 - 2(q_1^2 + q_2^2) \end{bmatrix}, \tag{3}$$

where the individual quaternions are obtained from the Euler angles [14].

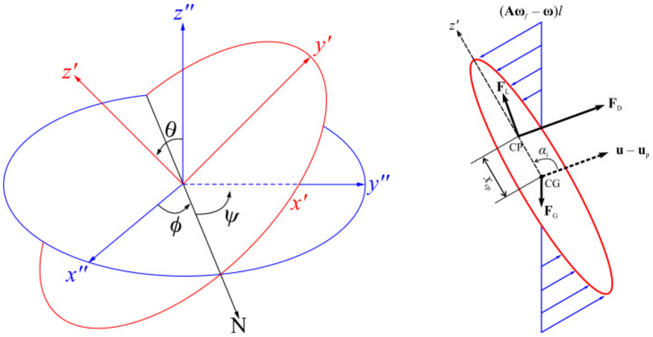

Fig. 1. Schematic of co-ordinate system and orientational angles of a particle with respect to particle major axis z' (left), and distance between centres of pressure (CP) and of mass (CM) of particle, x_{cp}, and incidence angle between ($\mathbf{u}$-$\mathbf{u}_{\mathrm{p}}$) and particle major axis z', α_i (right).

The forces, $\mathbf{F}$, and torques, $\mathbf{T}$, acting on a particle may change the momenta of a particle as expressed in Eq. (4):

$$\dot{x}(t) = \begin{pmatrix} \dot{\mathbf{x}} \\ \dot{\mathbf{q}} \\ \dot{\mathbf{P}} \\ \dot{\mathbf{L}} \end{pmatrix} = \begin{pmatrix} \frac{1}{m}\mathbf{P} \\ \frac{1}{2}\omega_q \mathbf{q} \\ \mathbf{F} \\ \mathbf{T} \end{pmatrix}, \tag{4}$$

where $\mathbf{x}$ is the position of its centre of mass**,** $\mathbf{q}$ is the quaternion describing its orientation, $\mathbf{P}$ is the linear momentum, $\mathbf{L}$ is the angular momentum, m is the mass of the body, and ω_q indicates a quaternion with scalar part 0 and a vector part with angular velocity $\boldsymbol{\omega}$. Note a boldfaced letter denotes a vector, and a dotted letter denotes a time derivative. For heavy particles ($\rho_p/\rho \gg 1$) the deterministic part taken from the Maxey and Riley formulation for the force was limited to the drag force, $\mathbf{F}_{\mathrm{D}}$, while the effect of other forces were neglected for the sake of improving fundamental understanding of fluid-particle interaction with a manageable parameter range. With the above simplifications, the drag force resulting from particle orientation is given, according to [14], as:

$$\mathbf{F}_{\mathrm{D}} = \tfrac{1}{2}\rho A_D C_D \,|\mathbf{u}-\mathbf{u}_p\,|(\mathbf{u}-\mathbf{u}_p)\,, \tag{5}$$

where $\mathbf{u}=(u,v,w)$ and $\mathbf{u}_p=(u_p,v_p,w_p)$ are the fluid velocity vector at the particle centre of mass and the particle velocity vector respectively and A_{D} is the particle area normal to the direction of the drag force. The projected area A_{D} can be expressed as a function of the particle incidence angle, α_i, between the particle slip velocity, ($\mathbf{u}-\mathbf{u}_p$), and the particle principal axis, z' (see Figure 1) as [14]:

$$A_{\mathrm{D}} = \pi a^2\left[\cos^2\alpha_i + \left(\frac{4b}{a\pi}\right)^2 \sin^2\alpha_i\right]^{\frac{1}{2}}, \tag{6}$$

where $A_D = \pi a^2$ for a spherical particle with $\lambda = 1.0$. The drag coefficient C_D has been measured for a wide range of particle shapes, but is not generally available in terms of a functional relationship with the Reynolds number, and the orientation and geometric parameters of the particle. One way to deal with this problem is by using the sphericity factor, S, and the volume equivalent diameter, d_{eq}, as geometric parameters and introducing orientation dependency in drag correlations using the effective area normal to the direction of the drag force. Here, following a review of available drag coefficient correlations [15], the Ganser [16] drag coefficient expression is used for C_D in Eq. (5), as given by:

$$\frac{C_D}{K_2} = \frac{24}{Re_p K_1 K_2}\left[1+0.118\left(Re_p K_1 K_2\right)^{0.6567}\right] + \frac{0.4305}{1+3305/(Re_p K_1 K_2)}\,, \tag{7}$$

where C_D and $\mathrm{Re}_p = |\mathbf{u}-\mathbf{v}|\, d_{eq}/\nu$ are based on the equal volume sphere diameter, d_{eq}, $K_1 = f_1(d_n, d_{eq}, S)$ and $K_2 = f_2(S)$ are the Stokes and Newton shape factors that model the particle sphericity and orientation, $d_n = (4A_D/\pi)^{1/2}$ is the equal-projected area circle diameter, and S is the particle sphericity, defined as the ratio of the surface area of a sphere having the same volume as the particle to the actual surface area of the non-spherical particle.

A stochastic Markov model is adopted to represent the influence of the unresolved fluid velocity fluctuations experienced by a stochastic particle p over a time, dt [12]. Adding the deterministic part, the drag term, $\mathbf{F}_{\mathrm{D}}$, and the stochastic (SGS dispersion) part together gives:

$$\mathrm{d}\mathbf{u}_p = (\mathbf{F}_{\mathrm{D}})\mathrm{d}t + \sqrt{(C_0 k_{sgs}/\tau_t)}\,\mathrm{d}\mathbf{W}_t\,, \tag{8}$$

where the last term in Eq. (8) models the SGS particle dispersion [12]; k_{sgs} is the unresolved kinetic energy of the fluid, C_0 is a model constant, $\mathrm{d}\mathbf{W}_t$ represents the increment of the Wiener process and τ_t is a sub-grid timescale which affects the rate of interaction between the particle and turbulence dynamics.

The rate of change with time of the principal components of the angular velocity $\boldsymbol{\omega} = (\omega_{x'}, \omega_{y'}, \omega_{z'})$ is given by the Euler equation rotation as:

$$I_a \frac{\mathrm{d}\omega_a}{\mathrm{d}t} = T_a + (I_b - I_c)\omega_b\omega_c\,, \tag{9}$$

where $(i,j,k) = (x',y',z')$, (y',z',x') and (z',x',y') are the principal components of the torque, $T_i = \mathbf{T}_H + \mathbf{T}_R$, with the moment of inertia, I_i, and the angular velocity, ω_i. The principal moments of inertia of a spheroid are $I_{x'x'} = I_{y'y'} = \frac{4}{15}\pi\lambda(\lambda^2+1)a^5\rho_p$ and $I_{z'z'} = \frac{8}{15}\pi\lambda a^5\rho_p$. The net torque $\mathbf{T} = [T_{x'}, T_{y'}, T_{z'}]$ acting on the particle is the sum of the hydrodynamic torque, $\mathbf{T}_H$, caused by the non-coincident centres of mass and of pressure, and the torque due to the resistance on a relatively rotating body, $\mathbf{T}_R$, which always acts to attenuate the relative spin. $\mathbf{T}_H$ and $\mathbf{T}_R$ are given in the particle frame of reference as [14, 17]:

$$\mathbf{T}_H = \mathbf{A}[(x_{cp}\mathbf{z}')\times(\mathbf{F}_D)]\,, \tag{10}$$

where $\mathbf{T}_H$ will change its sign, such that $\mathbf{T}_H = -\mathbf{T}_H$ when $\cos\alpha_i > 0$. The term x_{cp} is a semi-empirical expression proposed in [14] that defines the offset between the centres of mass and pressure. $\mathbf{T}_R$ can be directly derived by integration of the friction, caused by rotation, over the particle length, L. $\mathbf{T}_R$ for spheroidal particles within Stokes conditions is known [3] and has also been expanded to other shapes and to higher Reynolds numbers, with the local relative spin given as $(\mathbf{A}\boldsymbol{\omega}_f - \boldsymbol{\omega})$, and with $\boldsymbol{\omega}_f = \frac{1}{2}\nabla\times\mathbf{u}$ accounting for the undisturbed fluid vorticity at the point occupied by the particle's centre of mass [14, 17]. The resulting torque is thus expressed as:

$$\mathbf{T}_\mathrm{R} = \pm\int_0^{L/2} C_\mathrm{D}\rho_\mathrm{f} A_\mathrm{D}[(\mathbf{A}\boldsymbol{\omega}_f - \boldsymbol{\omega})l]^2\,\mathrm{d}l\,, \tag{11}$$

where the sign (±) of $\mathbf{T}_R$ is selected as the sign of $(\mathbf{A}\boldsymbol{\omega}_f - \boldsymbol{\omega})$, and l is the distance from the centre of rotation (see Figure 1). The time evolution of the quaternion is used to update the orientation of the particles and is computed as:

$$\dot{q} = \begin{pmatrix} \dot{q}_0 \\ \dot{q}_1 \\ \dot{q}_2 \\ \dot{q}_3 \end{pmatrix} = \frac{1}{2}\begin{bmatrix} q_o & -q_1 & -q_2 & -q_3 \\ q_1 & q_0 & -q_3 & q_2 \\ q_2 & q_3 & q_0 & -q_1 \\ q_3 & -q_2 & q_1 & q_0 \end{bmatrix}\begin{bmatrix} 0 \\ \omega_{x'} \\ \omega_{y'} \\ \omega_{z'} \end{bmatrix}. \tag{12}$$

Lastly, it should be noted that there is coupling between the translational and rotational motion. In Eq. (10), the torque due to the non-coincident centres of mass and of pressure, $\mathbf{T}_H$, is a function of the hydrodynamic force in the inertial frame which is transformed to the particle frame by the transformation matrix $\mathbf{A}$. For each time or integration step, the transformation matrix is obtained from the new quaternions, and these quaternions are subsequently used to obtain new values of α_i, A_D, d_n, C_D, F_D and $\mathbf{T}_R$. This is also the case for the torque due to the resistance on a relatively rotating body, $\mathbf{T}_R$, which is a function of A_D and C_D.

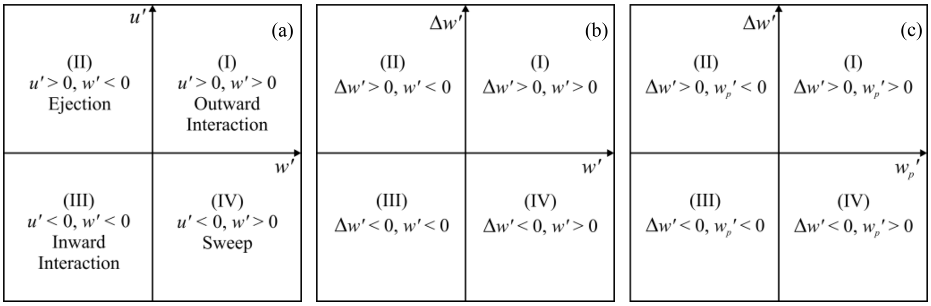

Fig. 2. Quadrant analysis of bursting process: (a) $u'w'$ Reynolds stress in $u' - w'$ space, (b) in $\Delta w' - w'$ space, and (c) in $\Delta w' - w'_p$ space.

3. Quadrant decomposition of velocity and slip velocity fluctuations

The bursting process consists of four categories of event; these categories are defined by the quadrant of the event as shown in Fig. 2. This categorisation is common for the fluid Reynolds stress between the streamwise (w') and wall-normal (u') velocity fluctuations [18] and this approach will be adopted for the fluid-particle interactions, i.e. the slip velocity fluctuation, $\Delta\mathbf{u}'$. The fluid, particle and slip velocity are largely dependent on the position within the boundary layer between the two parallel walls. Following Reynolds decomposition, the instantaneous fluid, particle and slip velocity vectors are decomposed into a mean part, $<\bullet>$, and a fluctuating part, $\bullet'$, given as:

$$\begin{gathered}\Delta\mathbf{u} = <\Delta\mathbf{u}> + \Delta\mathbf{u}' \\ <\Delta\mathbf{u}> = <\mathbf{u}> - <\mathbf{u}_p> \\ \Delta\mathbf{u}' = \mathbf{u}' - \mathbf{u}'_p\end{gathered} \tag{13}$$

The instantaneous fluid and particle velocity vectors are decomposed as $\mathbf{u} = <\mathbf{u}> + \mathbf{u}'$ and $\mathbf{u}_p = <\mathbf{u}_p> + \mathbf{u}'_p$, respectively. Note the parameters are both time- and spaced- averaged.

As show in Figure 2(a), a Q1 event ($u' > 0$ and $w' > 0$) corresponds to an outward motion of high-speed fluid away from the wall. A Q2 event ($u' > 0$ and $w' < 0$) describes an ejection of low-speed fluid into the high-speed stream. A Q3 event ($u' < 0$ and $w' < 0$) represents an inward motion of low-speed fluid towards the wall, while an event with ($u' < 0$ and $w' > 0$) falls into Q4 and describes the inrush of high-speed fluid into a low-speed region, also known as a sweep.

4. Numerical Simulations

The turbulent channel flow into which particles were injected was represented using a computational domain ($2h\times 2h\pi\times 4h\pi$) that was discretized with (129×128×128) nodes, where the ($x\times y\times z$) axes are in the wall normal, spanwise and streamwise directions, respectively. The Reynolds numbers $Re_\tau(= hu_\tau/v)$ and $Re_b(= hu_b/v)$ were 300 and 4910 based on the shear velocity, u_τ, and the bulk velocity, u_b, with the channel half height h, kinematic viscosity $v = 1.57\times 10^{-5}$ m^2 s^{-1} and density $\rho = 1.3$ kg m^{-3}. The shear velocity is defined as $u_\tau = (\tau_w/\rho)^{1/2}$, where τ_w is the mean shear stress at the wall. The mesh spacing was uniform in the y and z directions and non-uniform in the x direction. Periodic boundary conditions were used in the streamwise and spanwise directions, while no-slip boundary conditions were imposed at the walls. In the streamwise direction the mass flow was fixed, such that the driving pressure gradient which corresponds to the average wall shear stress for the computational domain at a given time had to vary. A dynamic time-step was chosen to ensure that Courant numbers were always less than 0.3. The solution was assumed to be statistically stationary when the driving pressure gradient was quasi-periodic in time. To avoid laminarisation of the flow, an initial simulation at high Reynolds number was carried out and the resulting solution used to initialize flow at $Re_\tau = 300$. Variables are reported in wall units, with superscript $^+$, by normalizing them by u_τ, and v.

A Lagrangian particle tracking code coupled with the LES code was developed [2], an extension of the work reported in [14] for ellipsoidal particles, and that of [9] for particles in a shear flow, to calculate particle trajectory, rotation and orientation in the flow field. The code interpolates fluid velocities at Eulerian grid nodes onto the particle position by means of trilinear interpolation, and integrates the equations of particle motion forward in time by means of a 4th order Runge-Kutta scheme. The particles are assumed to be pointwise, rigid and the shape is a function of the aspect ratio, $\lambda = c/a$, where a and c correspond to the particle semi-minor and semi-major axis lengths. Periodic boundary conditions are imposed on particles in both streamwise and spanwise directions. The particle wall boundary condition is straightforward for spherical and complex for non-spherical particles. Spherical particles are assumed to have contacted the wall when the distance from their centre of mass to the wall is less than the particle radius. However, for the ellipsoidal particles, three particle-wall collision scenarios could occur [5]. First, if the distance of the particle centroid from the boundary surface is less than the semi-minor axis, a, it has contacted the wall. Second, if this relative position is greater than the semi-major axis, c, the ellipsoid is in suspension. Third, when the distance between the particle centroid and the wall is within the range of the a and c axes, whether the ellipsoid is in contact with the wall or not depends on its orientation relative to the wall. The particle initial conditions are such that at the beginning of the simulation, particles are distributed randomly over the computational domain and their initial velocity and spin is set equal to that of the fluid at the particle position, while their initial orientation was obtain from randomly sampled Euler angles. The particle size (inertia) was measured using the equivalent volume diameter, d_{eq}, and a non-dimensional relaxation time, τ^+_{eq}. The equivalent volume diameter, d_{eq}, is defined as the diameter of the sphere with the same volume of the ellipsoidal particle, $d_{eq} = 2a\lambda^{1/3}$ and $\tau^{+}_{eq} = Sd^{+}_{eq}/18$, where $d^{+}_{eq} = d_{eq}u_{\tau}/\nu$.

5. Results and discussion

The LES results from a channel flow with Re_{τ} = 300 are first validated against DNS results [19] in Fig. 3(a) for the Reynolds normal stress terms ($u'^{+}_{\rm ms}$, $v'^{+}_{\rm ms}$ and $w'^{+}_{\rm ms}$) in the wall-normal, spanwise and streamwise directions. There is good agreement between the LES and DNS results which gives confidence in the present two-phase computations. By using quadrant analysis analogous to Fig. 2(a), Fig. 3(b) shows how each quadrant's events contribute to the distribution of the shear stress term $< u'w' >$ as a function of the non-dimensional wall-normal location, x^{+}. Note, the exact expression for the Reynolds stress is $(-\rho u'w')$. The first (Q1) and third (Q3) quadrants contribute to the negative Reynolds shear stress while the second (Q2) and fourth (Q4) quadrants show positive turbulence production. The intensity of sweep events dominates at $x^{+} \le 22$, while that of ejection events is greatest away from the wall, at $x^{+} > 22$. These results are consistent with other findings reported in the literature [18, 20], where it has been show that the magnitude of the turbulent velocity fluctuations in the three directions peaks in the buffer region ($5 < x^{+} < 30$), with the region being dominated by strong Q2 and Q4 events.

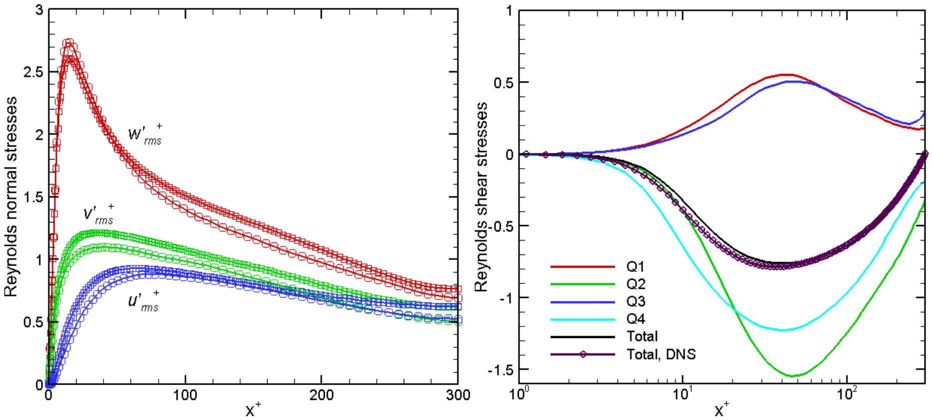

Fig. 3. (a) Reynolds normal stresses (linear-linear scale, squares – DNS, circles – LES), and (b) Reynolds shear stress <*u'w'*> from each quadrant (log-linear scale) normalised by the friction velocity, for the single-phase flow.

Next, results based on the probability density function (PDF) of the fluctuating velocities at the particle position are presented. Two hundred thousand particles with density $\rho_p = 1000$ kg m^{-3} and three shapes based on aspect ratio, representing a disk $(\lambda = 0.1)$, a sphere $(\lambda = 1)$ and a needle $(\lambda = 10)$ following the Loth [21] classification, were tracked in the flow to analyse the shape and orientation effect on particle segregation. Note, the three shaped particles have an equal equivalent volume diameter d_{eq} but different sphericity due to their different aspect ratios. A great deal of results were generated from this study, although only the results for non-dimensional particle response time based on an equivalent volume diameter $\tau^{+}_{eq} = 25$ are reported in this paper. Other statistical analyses for the full range of parameters studied ($Re_{\tau}, \tau^{+}_{eq}, \lambda, x^{+}$) will be provided in the future.

Instantaneous scatter plots of the non-dimensional streamwise slip velocity fluctuation ($\Delta w'^{+}$) versus the non-dimensional fluid streamwise fluctuating velocity, (w'^{+}), are shown in Fig. 4, and versus the non-dimensional particle streamwise fluctuating velocity, (w'^{+}_{p}), in Fig. 5, where results for the disk, sphere and needle particles are given. Note that the superscript ($^{+}$) has been omitted from the figures and subsequent text for simplicity. The statistical analyses presented in Fig. 4 and Fig. 5 were obtained from conditional averaging rather than averaging over discrete Eulerian grid points. Four hundred samples at intervals of 100 time steps at buffer region wall-normal positions, $7 \le x^{+} \le 9$, and subjected to the quadrant analyses based on Fig. 2(b) and 2(c), respectively, are considered. The percentage figures given in Fig. 4 and Fig. 5 are the time-averaged percentage values of the quadrant distributions. Similarly, the time-averaged percentage values of the quadrant distributions are also shown in Table 1 for the same analysis applied in the wall-normal direction, u . The asymmetric distributions in the ($\Delta w', w'$)- and ($\Delta w', w'_p$)-planes show non-homogeneity in the particle segregation in the near-wall region. The maximum positive slip velocity ($\Delta w'$) was obtained when $w' > 0$ in Fig. 4 and when $w'_p < 0$ in Fig. 5. Similarly, the maximum negative slip velocity ($\Delta w'$) was obtained when $w' < 0$ in Fig. 4 and when $w'_p > 0$ in Fig. 5. Interestingly, in both figures, and in the results of Table 1, there is a common trend. For events with alternating sign between $\Delta w'$ and w'_p or w' (i.e. Q2 and Q4), the Q2 (ejection) events are more frequent than the Q4 events at this sampling location, $7 \le x^+ \le 9$. Note that the Q4 events ($\Delta w' < 0, w' > 0$) of Fig. 4 represent highly intermittent particle-to-fluid motions in high-speed fluid streaks. Similarly, for events with the same sign between $\Delta w'$ and w'_p or w' (i.e. Q1 and Q3), the Q3 (inward interaction) events are more frequent than the Q1 events at the same sampling location. This tread will change when the statistics are sampled at other boundary layer locations, especially away from the near-wall region, as well as for different particle inertia.

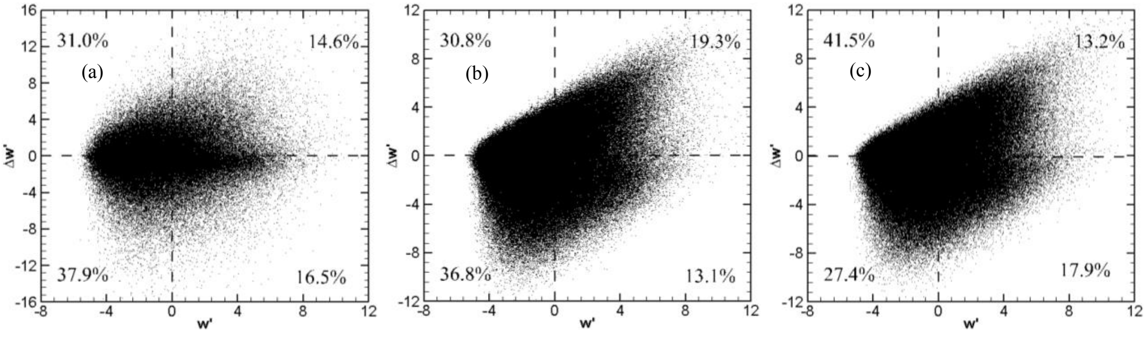

Fig. 4. Scatter plots of the fluid streamwise velocity fluctuation, w' , and streamwise slip velocity fluctuation, $\Delta w'$, for a) a disk (λ = 0.1), (b) a sphere (λ = 1.0) and (c) a needle (λ = 10), all with equivalent relaxation time $\tau^+_{eq} = 25$ and conditionally sampled particle wall normal positions $x^+ = 7 - 9$. For comparison purposes, a percent value corresponding to the number of particles in each quadrant is provided.

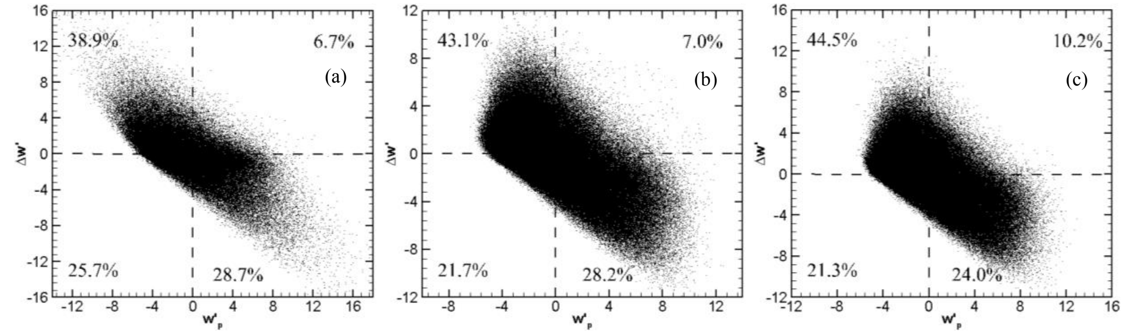

Fig. 5. Scatter plots of the particle streamwise velocity fluctuation, w'_p , and the streamwise slip velocity fluctuation, $\Delta w'$, for (a) a disk (λ = 0.1), (b) a sphere (λ = 1.0) and (c) a needle (λ = 10), all with equivalent relaxation time $\tau^+_{eq} = 25$ and conditionally sampled particle wall normal positions $x^+ = 7 - 9$. For comparison purposes, a percent value corresponding to the number of particles in each quadrant is provided.

In Fig. 4, showing the ($\Delta w', w'$)-plane, the summation of Q2 and Q3 events, representing events with a negative streamwise fluid velocity fluctuation $w' < 0$, accounts for up to 70% of the reported events. This trend holds for all three shapes of particle. This means that, regardless of the particle shape, particles with finite inertia tend to preferentially concentrate in low-speed streaks that dominate the near-wall regions. Furthermore, the fractions of the number of events in each of the four quadrants is similar for particles with aspect ratios $\lambda \le 1.0$. In contrast, for the distributions in Fig. 5 that shows the ($\Delta w', w'_p$)-plane, the fractions of the number of events in each of the four quadrants are similar for particles with aspect ratios $\lambda \geq 1.0$. In Fig. 5, the summation of Q2 and Q4 events dominates and totals to approximately 70% of the overall events. Particles with a tendency to preferentially concentrate in low-speed streaks are therefore likely to encounter the wall and, if the energy barrier is overcome, to deposit on the wall surface. A similar analysis can be performed in terms of the correlation of the wall-normal slip velocity fluctuation with the wall-normal fluid velocity fluctuation ($\Delta u', u'$), and the wall-normal slip velocity fluctuation with the particle wall-normal velocity fluctuation ($\Delta u', u'_p$), as presented in Table 1.

Lastly, Figure 6 shows the probability density function of the non-dimensional streamwise fluid velocity fluctuations, PDF(w'^+), sampled again in the buffer region, at $7 \leq x^+ \leq 9$, and conditionally sampled for particles with positive ($\Delta w' > 0$) and negative ($\Delta w' < 0$) streamwise slip velocity fluctuation values. This figure is intended to give more insight into the role of particle slip velocity fluctuations in particle segregation behaviour in the near-wall region of a turbulent channel flow. The shape of the distributions are similar for the three shapes of particle with $\tau_{eq}^+ = 25$. Hence, for the range of particle aspect ratios considered, the spatial distribution of the particles conditionally sampled at $7 \leq x^+ \leq 9$ is skewed, with all three particle shapes having peaks in the PDF(w'^+) at $w' < 0$. This is the region where the local fluid velocity is lower than the mean fluid velocity at the particle position. The peak of the PDF(w'^+) of particles with $\Delta w' < 0$ is also larger than that for $\Delta w' > 0$, suggesting that a larger number of particles lag the local fluid motion, and that their dispersion is strongly depended on the drag force.

Table 1. Percent particle counts for each ($u', \Delta u'$) quadrant (left) and ($u'_p, \Delta u'$) quadrant (right).

λ	($\Delta u', u'$) Quadrant		($\Delta u', u'_p$) Quadrant	
	Q2	Q1	Q2	Q1
0.1	23.5%	27.2%	31.0%	14.6%
1.0	20.3%	28.4%	30.8%	19.3%
10	19.1%	24.6%	41.5%	13.2%
	Q3	Q4	Q3	Q4
0.1	23.3%	26.0%	37.9%	16.5%
1.0	30.8%	20.5%	36.8%	13.1%
10	34.5%	21.8%	27.4%	17.9%

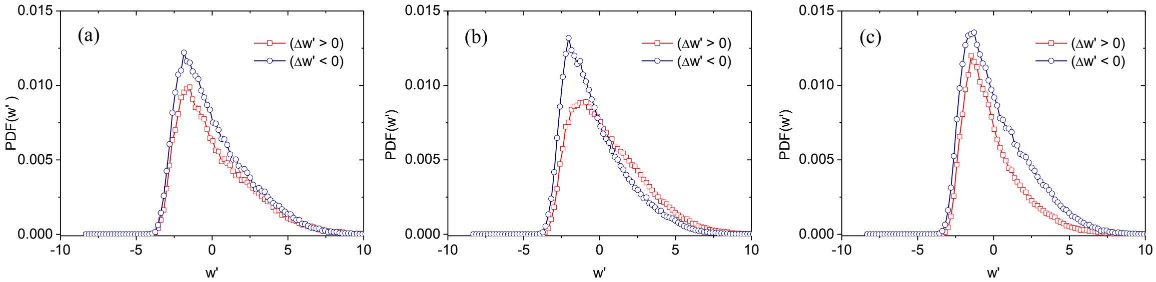

Fig. 6. Effect of particle aspect ratio on conditioned PDF(w') for particles with streamwise $\Delta w' > 0$ and $\Delta w' < 0$ for a) disk (λ = 0.1), (b) sphere (λ = 1.0) and (c) needle (λ = 10).

6. Conclusions

In this paper, particle segregation has been studied using large eddy simulation, Lagrangian particle tracking and a conditional statistical analyses of particle and fluid velocity fields in a turbulent channel flow with shear Reynolds number $Re_\tau = 300$. One-way coupling was adopted and only the drag force and the contribution from the unresolved sub-grid scale of the velocity fluctuations on particle acceleration was accounted for. Particles with aspect ratios of $\lambda = 0.1$, 1.0 and 10, representing a disk, a sphere and a needle, were simulated. The three shaped particles had an equal equivalent volume diameter and non-dimensional particle relaxation time, $\tau_{eq}^{+} = 25$. The particle interaction with near-wall turbulent coherent structures (outward motion, ejection, inward motion and sweep) was analysed by using conditional statistics (probability density function and scatter plots) in quadrants to study the distribution of the fluid, particle and slip velocity fluctuations. The results showed that, regardless of their shape, all the particles tend to preferentially concentrate in low-speed streaks within the near-wall region.

Acknowledgements

The authors wish to thank the Engineering and Physical Sciences Research Council for their financial support of the work reported in this paper under EPSRC Grant EP/I003010/1, “Computational Modelling for Advanced Nuclear Power Plants”.

References

[1] C. Marchioli, A. Soldati, Mechanisms for particle transfer and segregation in a turbulent boundary layer, J. Fluid Mech. 468 (2002) 283-315.
[2] D.O. Njobuenwu, M. Fairweather, Non-spherical particle translation and orientation in wall-bounded turbulence, in: T.E. Simos, G. Psihoyios, C. Tsitouras (Eds.) 11th International Conference on Numerical Analysis and Applied Mathematics 2013 (ICNAAM-2013), AIP Conference Proceedings, Rhodes, Greece, 2013, pp. 132-135.
[3] G.B. Jeffery, The motion of ellipsoidal particles immersed in a viscous fluid, P. Roy. Soc. Lond. A Mat. 102 (1922) 161-179.
[4] F.P. Bretherton, The motion of rigid particles in a shear flow at low Reynolds number, J. Fluid Mech. 14 (1962) 284-304.
[5] F.-G. Fan, G. Ahmadi, A sublayer model for wall deposition of ellipsoidal particles in turbulent streams, J. Aerosol Sci. 26 (1995) 813-840.
[6] H. Zhang, G. Ahmadi, F.-G. Fan, J.B. McLaughlin, Ellipsoidal particles transport and deposition in turbulent channel flows, Int. J. Multiphas. Flow 27 (2001) 971-1009.
[7] P.H. Mortensen, H.I. Andersson, J.J.J. Gillissen, B.J. Boersma, Dynamics of prolate ellipsoidal particles in a turbulent channel flow, Phys. Fluids 20 (2008) 093302.
[8] C. Marchioli, M. Fantoni, A. Soldati, Orientation, distribution, and deposition of elongated, inertial fibers in turbulent channel flow, Phys. Fluids 22 (2010) 033301.
[9] D.O. Njobuenwu, M. Fairweather, Effect of shape on inertial particle dynamics in a channel flow, Flow Turbul. Combust 92 (2014) 83-101.
[10] L.H. Zhao, C. Marchioli, H.I. Andersson, Stokes number effects on particle slip velocity in wall-bounded turbulence and implications for dispersion models, Phys. Fluids 24 (2012) 021705.
[11] U. Piomelli, J. Liu, Large-eddy simulation of rotating channel flows using a localized dynamic model, Phys. Fluids 7 (1995) 839-848.
[12] M. Bini, W.P. Jones, Large-eddy simulation of particle-laden turbulent flows, J. Fluid Mech. 614 (2008) 207-252.
[13] H. Goldstein, Classical Mechanics, 2nd ed., Addison-Wesley, Reading, MA, 1980.
[14] C. Yin, L. Rosendahl, S. Knudsen Kær, H. Sørensen, Modelling the motion of cylindrical particles in a nonuniform flow, Chem. Eng. Sci. 58 (2003) 3489-3498.
[15] R.P. Chhabra, L. Agarwal, N.K. Sinha, Drag on non-spherical particles: an evaluation of available methods, Powder Technol. 101 (1999) 288-295.
[16] G.H. Ganser, A rational approach to drag prediction of spherical and nonspherical particles, Powder Technol. 77 (1993) 143-152.
[17] C. Yin, L. Rosendahl, S. K. Kær, T. J. Condra, Use of numerical modeling in design for co-firing biomass in wall-fired burners, Chem. Eng. Sci. 59 (2004) 3281-3292.
[18] J. Kim, P. Moin, R. Moser, Turbulence statistics in fully developed channel flow at low Reynolds number, J. Fluid Mech. 177 (1987) 133-166.
[19] C. Marchioli, A. Soldati, Reynolds number scaling of particle preferential concentration in turbulent channel flow, in: J.M.L.M. Palma, A.S. Lopes (Eds.) Advances in Turbulence XI, Springer Berlin Heidelberg, 2007, pp. 298-300.
[20] J. Huang, Y. Murai, F. Yamamoto, Quadrant analysis of bubble induced velocity fluctuations in a transitional boundary layer, J. Hydrodyn. Ser. B 21 (2009) 93-99.
[21] E. Loth, Drag of non-spherical solid particles of regular and irregular shape, Powder Technol. 182 (2008) 342-353.